Stress Recovery for the Particle-in-cell Finite Element Method

Authors: Haibin Yang[1], Louis N. Moresi[1,2], John Mansour[3]

Affiliation 1: School of Earth Sciences, University of Melbourne, Melbourne, Australia

Affiliation 2: Research School of Earth Sciences, Australian National University, Canberra, Australia

Affiliation 3: Monash eResearch Centre, Monash University, Clayton, Australia

Corresponding Author: Haibin Yang

Email: haibiny@student.unimelb.edu.au

Abstract

The interelement stress in the Finite Element Method is not continuous in nature, and stress projections from quadrature points to mesh nodes often causes oscillations. The widely used particle-in-cell method cannot avoid this issue and produces worse results when there are mixing materials of large strength (e.g., viscosity in Stokes problems) contrast in one element. The post-processing methods including (1) distance weighted average from surrounding particles to the centroid mesh node (Post-local), (2) global projection with least square fit (Post-global), and (3) superconvergent point recovery method (SPR), cannot effectively eliminate the stress fluctuations. We propose three pre-processing methods to reduce the interface contrast in mixing elements: (1) global method with harmonic-mean averaging (GHM), (2) unification of properties at mixed-material elements (UnE), and (3) averaging particle properties within a specified distance to gauss quadrature points (AGP). For tests of Q_1 elements, the results processed by combining either pre-processing method with the Post-local projection can increase the precision. The GHM pre-processing method is the least computationally expensive application and the easiest to implement, the AGP pre-processing method is the most expensive and the UnE in-between. However, for Q_2 elements, the GHM pre-processing method fails in stress recovery, and produces worse results than those without any pre-processing procedures. For general cases (both Q_1 and Q_2 elements), the AGP pre-processing method is recommended. The optimal sampling radius used in the AGP method is close to that size of one element, beyond which it increases computational time, but does not significantly increases the accuracy of recovered stresses. In terms of the averaging approaches used in the AGP method, the harmonic mean is suitable for simple-shear-dominated processes and the arithmetic mean is better for the pure-shear-dominated models. For complex models, the AGP method of harmonic mean combined with the SPR post-procedure is recommended. The AGP method is found to be able to efficiently reduce stress perturbations in a synthetic model of complex fault geometries like the San Andreas Fault system.

Key words:

Particle-in-cell; Finite Element Method; Stress fluctuation; Stress smoothing; Numerical geodynamic modelling

1 Introduction

The classical Finite Element Method (FEM) (see e.g. Hughes (2012)) has been widely used to simulate different structures in engineering. Different from most engineering problems, geological simulations are challenged by emergent structures due to the non-linear processes involved (Lenardic et al., 2003). For the body fitted FEM meshes, the modelled system evolving with large deformations distorts meshes, which may produce more complexities (like re-meshing) in computation (Braun and Sambridge, 1994). Alternatively, the particle-in-cell (PIC) method allows Lagrangian material particles to move in a background Eulerian mesh (Harlow, 1964; Sulsky et al., 1994). Those particles carry information of density, composition, viscosity, etc., while the unknowns are solved at nodes of the mesh.

One disadvantage of the PIC FEM is that large deformation causing mixing of materials of great strength contrast in one cell triggers oscillations of stresses along the cell edges. For Stokes problems, this strength property generally refers to viscosity. The jump of viscosity in one element is found to give rise to an error more than two orders of magnitude larger than ones with material interfaces aligned with element boundaries (Moresi et al., 1996). This viscosity jump can also significantly degrade convergence rate of numerical solvers (May and Moresi, 2008).

To avoid this mixing effect, Wallstedt and Guilkey (2011) suggested a weighted least square particle-in-cell method to project materials properties to nodes, which requires subdivision of the mixed-material cell. They integrals those particles of same properties separately. To save the computational time of dividing the integration domain, Sadeghirad et al. (2011) tried new basis functions over particle field using a 4-node finite element interpolation method and the integration is based on each particle in the corresponding element rather than on gauss quadrature points, which can be implemented in the mantle convection models in a simple and efficient way (Moresi et al., 2003). While this may work well for simple 2D problems, its efficiency of implementation for complex geological problems is not sufficiently studied.

There are some other, simpler methods, which directly manipulate the property distribution in one element. Averaging of the viscosity in cells with multi-phase materials in the Finite Difference Method is systematically studied by Deubelbeiss and Kaus (2008). However, for the case of the Finite Element Method, they simply put a single value for all quadrature point in one element to avoid viscosity jump. This constant interpolation of viscosity in the cell with mixed materials is also tested by Thielmann et al. (2014), who proposed another more sophisticated strategy, the linear least square interpolation, which requires solving a linear equation for each mixed-material element. However, this extra cost of combining linear least square interpolation with Q_2 element does not work well in cases of sharp changes of viscosity in one element (Thielmann et al., 2014).

This work examines several smoothing methods to eliminate spurious stress fluctuations in the framework of Underworld2, which is a Python application programming interface to simulate geodynamics processes (https://github.com/underworldcode/underworld2) (Moresi et al., 2007). The smoothing methods we test can be conveniently implemented and efficiently run with Underworld2. We first introduce two post-processing methods available in Underworld2, and then describe three pre-processing solutions: (1) a global method with harmonic-mean averaging, (2) unifying material properties at elements with mixed materials, and (3) averaging at gauss quadrature points, which, in the remainder of this context, are referred to as GHM, UnE, and AGP respectively. Additionally, we further compare them with the classical stress recovery technique that reconstruct continuous stresses on specified patches based on super-convergent points inside the elements (SPR) (Zienkiewicz and Zhu, 1992a, b). The SPR method is for cases without the internal structure in the element, so they are not intended to alleviate the problem caused by mixed-material elements. The effect of each method is checked with geological models that have analytical solutions. Combining effects of different pre- and post-processing methods are also present. Finally, we investigate a synthetic model with relatively complex fault geometries based on the fault data from the San Andreas Fault system.

2 Governing equations

The simulation is based on the Stokes equation for Newtonian viscous, incompressible flow:

$$\frac{\partial \sigma_{ij}}{\partial x_j} - \frac{\partial P}{\partial x_i} = \rho g_i \quad (1)$$

$$\frac{\partial v_i}{\partial x_i} = 0 \quad (2)$$

$$\dot{\sigma}_{ij} = 2\eta \dot{\varepsilon}_{ij} \quad (3)$$

$$\dot{\varepsilon}_{ij} = \frac{1}{2}\left(\frac{\partial v_i}{\partial x_j} + \frac{\partial v_j}{\partial x_i}\right) \quad (4)$$

where σ_{ij} denotes deviatoric stress, P pressure, ρ density, g_i gravity acceleration, v_i velocity, η Newtonian viscosity, $\dot{\varepsilon}_{ij}$ strain rate, and the Einstein summation convention is used here.

3 Methods

3.1 Post-processing methods

For the classical Finite Element Method, inter-element stress continuity is not guaranteed. Smoothing the numerical discontinuity to fit the physically continuous system has been conventionally implemented as a post processing step. These generally include (1) averaging around local nodes and (2) global projection with least square fits. In this study, they are taken as the Post-local and Post-global projections, respectively (Hinton and Campbell, 1974).

3.1.1 Post-local - averaging around local nodes

The projection at mesh nodes is done through extrapolation from superconvergent points (e.g., Gauss points) and then averaging locally at mesh nodes. In the FEM framework, the distance-based weight can be achieved through the shape function (N_a) in the whole calculation domain Ω, so the average nodal stress

$$\sigma^h = \frac{\int N_a \sigma^p \, d\,\Omega}{\int N_a \, d\,\Omega} \tag{5}$$

where σ^p is the point stress. Note that, although the integration is applied to the whole domain, the shape function is zero outside adjacent elements.

3.1.2 Post-global - global projection with least square fits

The error between the smoothed stresses $\tilde{\sigma}$ and the point stresses σ^p is

$$\int (\tilde{\sigma} - \sigma_p)^2 \, d\Omega \tag{6}$$

The smoothed stress is written as

$$\tilde{\sigma} = \sum_{B=1}^{n_{np}} N_B \sigma_B^h \tag{7}$$

where n_{np} is the number of nodal points. The least square method is used to minimize the error by

$$\frac{\partial}{\partial \, \sigma_B^h} \int (\tilde{\sigma} - \sigma_p)^2 \, d\Omega = 0 \tag{8}$$

for $B = 1, 2, \ldots, n_{np}$. This yields the following matrix problem:

$$\boldsymbol{X}\tilde{\boldsymbol{\sigma}} = \boldsymbol{P} \tag{9}$$

where $\boldsymbol{X} = [X_{\boldsymbol{AB}}]$, $\tilde{\boldsymbol{\sigma}} = < \sigma_B^h >$ and $\boldsymbol{P} = < P_A >$.

The construction of $\boldsymbol{X}$ and $\boldsymbol{P}$ is implemented in the elementwise fashion:

$$x_{ab}^e = \int_{\Omega_e} N_a^e N_b^e d\Omega \,, \qquad p_a^e = \int_{\Omega_e} \sigma_p N_a^e d\Omega \tag{10}$$

for $1 \leq a, b \leq n_{en}$, where n_{en} is the number of nodal points per element.

The global projection method is a more costly process to recover accurate nodal stresses and sometimes produces overshoot values at nodal points.

3.1.3 SPR-superconvergent point recovery

The SPR method (Zienkiewicz and Zhu, 1992a) compute a continuous nodal stress field, σ^*, from a patch of elements local to each node:

$$\sigma^* = \boldsymbol{M}\,\boldsymbol{a} \tag{11}$$

where $\boldsymbol{M} = [\mathbf{1}, x, x^2, \ldots, x^m]$ and $\boldsymbol{a} = [a_1, a_2, a_3, \ldots, a_{m+1}]^{\boldsymbol{T}}$ for one dimensional cases. m is the order of the polynomial expansion, which is the same as that used in the shape function N. Accordingly, for the two-dimensional expansion for linear elements, $\boldsymbol{M} = [1, x, y]$, and for quadratic $\boldsymbol{M} = [1, x, y, x^2, xy, y^2]$ (the xy term is optional).

To determine the unknown parameters $\boldsymbol{a}$ in equation (11), we minimize

$$\boldsymbol{F} = \sum_{i=1}^{n} (\sigma_i^h(x_i, y_i) - \boldsymbol{M}(x_i, y_i)\boldsymbol{a})^2 \tag{12}$$

where (x_i, y_i) are the coordinates of specified sampling points, the total number of which is n. Therefore, for $\boldsymbol{F}$ to be a minimum

$$\frac{\partial \boldsymbol{F}}{\partial \boldsymbol{a_i}} = 0 \tag{13}$$

This gives

$$\sum_{i=1}^{n} \boldsymbol{M}^{\mathrm{T}}(x_i, y_i)\boldsymbol{M}(x_i, y_i)\boldsymbol{a} = \sum_{i=1}^{n} \boldsymbol{M}^{\mathrm{T}}(x_i, y_i)\, \sigma^h(x_i, y_i) \tag{14}$$

This system is rewritten as

$$\boldsymbol{a} = \boldsymbol{A}^{-1}\boldsymbol{b} \tag{15}$$

where

$$\boldsymbol{A} = \sum_{i=1}^{n} \boldsymbol{M}^{\mathrm{T}}(x_i, y_i)\boldsymbol{M}(x_i, y_i) \text{ and } \boldsymbol{b} = \sum_{i=1}^{n} \boldsymbol{M}^{\mathrm{T}}(x_i, y_i)\, \sigma^h(x_i, y_i) \tag{16}$$

After obtaining the parameter $\boldsymbol{a}$ in equation (11), with the polynomial expansion, the nodal values can be evaluated by any given coordinates to the functional form of σ^* in equation (11).

3.2 Pre-processing method

The classical post-processing methods are designed to produce continuous, node-based stress field, but not to resolve the stress perturbations caused by mixed-material elements. Instead, we utilize pre-processing methods to reduce the strength contrast across the interfaces between two materials. The Post-local method is taken as the default post-processing procedure that projects stress from particles to nodes after one specific pre-processing method. Any other post-processing method is stated when used in this study.

3.2.1 GHM - global method with harmonic-mean averaging

We use the method described in section 3.1.1 to project reciprocals of the property information η^p (e.g., viscosity) carried by particles to mesh nodes through the shape function (N_a) in the whole calculation domain Ω, so the harmonic mean viscosity

$$\eta^h = \frac{1}{\frac{\int N_a \ (1/\eta^p) \ \ d\Omega}{\int N_a \, d\,\Omega}} \tag{17}$$

The strength values η^*considered in the elementwise integration is

$$\eta^* = \sum_{A=1}^{n_{np}} N_A \eta_A^h \tag{18}$$

3.2.2 UnE - unification at one element

Here we first look for elements that contain more than one material, and then unify the properties of all the particles in those elements to be one value. The harmonic mean method averaging over all types of points in one cell , gives the unified property value

$$\eta^e = n_k / \sum_{A=1}^{n_k} 1/\eta_A^p \tag{19}$$

where n_k is the number of material types in one element. It is worthwhile noting that n_k is not the number of particles in one element. For large viscosity jump > 10^3 $\mathrm{Pa \cdot s}$, if the particles numbers in one cell is few (e.g. 10s), the effective viscosity for both cases are the same order of magnitude. For simplicity, we take the number of material types. The averaging over the number of particles is introduced in the next section.

3.2.3 AGP-averaging at Gauss quadrature points

This method is also applied only to elements with a mixture of materials, and we first locate mixed-material cells. Then, instead of unifying materials over one cell, particles within distance δ to the selected Gauss quadrature point are averaged by

$$\eta^{gp} = n_{dp} / \sum_{A=1}^{n_{dp}} 1/\eta_A^p \tag{20}$$

where n_{dp} is the number of sampling points for the specified Gauss quadrature point. The sampling numbers n_{dp} is determined by the selected distance δ. The effect of sampling distance is discussed later. The default averaging method is harmonic mean as shown in equation (21), and other averaging methods are stated when used.

4 Results and discussion

4.1 Models with analytical solutions

4.1.1 Simple shear model

We first test the effect of different smoothing methods by a simple shear model. Details of the setup is shown in Fig. 1a. A narrow weak zone ($\eta_2 = 10^{18}\,\mathrm{Pa\cdot s}$) is embedded in the background of high viscosity ($\eta_1 = 10^{20}\,\mathrm{Pa\cdot s}$). With the top boundary fixed, the driving velocity V_0 at bottom is 1 cm yr^{-1}, and periodic boundary conditions are applied to the left and right boundary. The model size is 20 km×20 km. Rectangular meshes with Q_1 elements of 40×40, 80×80, 160×160, and 320 ×320 are compared. The thickness of the weak zone is $h_2 = 2 \times 1.9\, dy$, where dy is one element length in y direction for the element resolution of 40×40, and the thickness of the weak zone does not change with mesh resolution. The weak zone is centered at y = 0, so neither interface (at $\pm 1.9\ dy$) is aligned with element edges. Taking the solution of Couette flow and considering stress continuity at both interfaces, we give the analytical results for shear stress

$$\sigma_{xy} = \frac{V_0 \eta_1}{h_3 + h_1 (\frac{h_2 \eta_1}{h_1 \eta_2} + 1)} \tag{21}$$

The results of 80×80 element resolution are shown in Fig. 1b-1f. The simple shear model should produce a homogeneous stress field, and the exact value from the analytical model is $10^{5.18}$ Pa. We define the normalized relative error

$$\mathrm{err} = \frac{f - f_0}{f_0} \tag{22}$$

where f is the nodal value from numerical models and f_0 is the corresponding analytical solution at the same point. In this simple shear model, f_0 = $10^{5.18}$ Pa. The mixing effect is obvious in the default output with Post-local projection (averaging around local nodes) (Fig. 1b), which results in fluctuations in stress error from -24.6 % to 78.0 %. We note that the fluctuations in Post-local projections are interpolated results from the raw values in particles, as the equation (5) does. We check the stresses at particles and found the same spurious stresses along interfaces (not shown in figures). Directly applying the superconvergent point recovery (SPR) method on the Post-local stress field, the resulted relative error range is reduced to 9.9 % – 36.7 % (Fig. 1c). We implement the pre-processing method to degrade stress perturbations. For the GHM pre-processing method, the relative error is -10.4 % – 28.1 %

(Fig. 1e). Further applying the SPR post-processing method on the GHM results, we find the relative error range is narrowed to -4.0 % – 14.5 % (Fig. 1f). In contrast, the UnE pre-processing method leads to a nearly homogeneous stress field as we expect, but it is about 8 % higher than the analytical solution (Fig. 1d).

To have a better understanding of the resolution controls on the numerical results accuracy, we define the mean error

$$\mathrm{Err} = \frac{\sqrt{\sum_{i=1}^{n} err^2}}{n} \tag{23}$$

where n is the number of nodal values in a specified area. We select nodes in a rectangular domain $-3.4\,dy < y < 3.4\,dy$, which covers the area of intensive oscillations. The resolution test (Fig. 2a) demonstrates that the errors decrease by three orders of magnitude for all applied smoothing methods. Additionally, we find the Post-global projection (global projection with least square fits) has slightly lower accuracy than the Post-local (averaging around local nodes) method. The errors in both the GHM and UnE pre-processing methods are about one order of magnitude less than Post-local projection results. Additionally, we define a parameter to describe the relative fluctuation range

$$flt = \frac{max(\boldsymbol{f}) - min(\boldsymbol{f})}{mean(\boldsymbol{f})} \tag{24}$$

where $\boldsymbol{f}$ is a group of all nodal values in a specified domain. The fluctuation ranges do not decrease dramatically (Fig. 2b) as the error does, while the grid resolution increases from 40 to 320. Using the SPR post-processing method to further process GHM results can help reduce fluctuation ranges by 10 %. Generally, the UnE post-processing method produces a much narrower fluctuation range than other results, because we unify the viscosity values in those mixed-material elements in the simple shear model. We note that the high efficiency of the UnE method is limited to special cases, like the simple shear model with material interfaces parallel to shear directions.

For the AGP pre-processing method (averaging at Gauss quadrature points), we test several models with different δ (the sampling radius of the circle centering at Gauss points in mixed-material elements). Fig. 3 shows results of a model (80×80) after the AGP pre-processing procedure. With sampling radius increasing from 0.5dx to 4dx, where dx is one element length, the relative error ranges of stress field perturbations decrease from -8.4 % – 22.9 % to 4.4 % – 9.9 %. The perturbation ranges should reduce with further increasing sampling radius, since, in the extreme case of a global scale averaging, it nearly produces a unified property in those mixing elements, thus yielding the same effect as the UnE pre-processing method. We note that the computation time for the UnE pre-processing method also increases with search area.

Q_2 elements are also tested to investigate how efficiently each method is in reducing stress perturbations (Fig. 4), which are more severe for Q_2 elements than the Q_1 cases. The Post-local projection produces relative errors of -99.6 % – 243.6 % (Fig. 4a) . The GHM method yields the worst result (err = -99.8 % – 3047.5 %; Fig. 4b), which is markedly worse than the Post-local projection. The UnE method can still generate uniform stress field (Fig. 4c), and the relative error (~ 8 %) is close to that in Q_1 cases in Fig 1d. The stress processed by the AGP method with sampling radius of 1dx dampens most of the noise to a much lower level (-0.2 % – 7.5%) than the Post-local and GHM methods (Fig. 4d). In the next step, the SPR method is utilized to do further post-processing of those results from Fig. 4a-4d. The SPR method reduces stress perturbations by more one order of magnitude for the Post-local solution (Fig. 4e). Although upper bound of the error after applying SPR on GHM results degrades by about one order of magnitude, the error ranges still have more than two orders of magnitude in spurious stress oscillation (Fig. 4f).

4.1.2 Folding model

Although the simple shear model has illustrated some features of different methods, models with a relatively complex geometry and boundary conditions may help us learn more about the broader applicability of those methods. We use the folding model from Ramberg (1962) as a benchmark. The model investigates contact strain in an incompetent host rocks adjacent to a buckling thin sheet that is composed of competent rocks. Mathematically, the competent buckling rock is treated as a very viscous Newtonian material (10^{22} Pa·s), while the background incompetent rock is of lower viscosity (10^{18} Pa·s) than the embedded rock. The geometry of the buckling sheet is described by a sinusoidal function

$$y = y_0 \sin\frac{2\pi x}{\lambda} \tag{25}$$

where y is the deflection of the center line of the thin sheet, y_0 the amplitude and λ the wavelength (Fig. 5). In the physical analysis, the thickness of the thin layer is assumed to be extremely small relative to its wavelength. We simulate a domain of 20 km × 20 km with the Q_1 element resolution of 320 × 320. The thickness of the thin layer (0.125km) spans 2 gird size (3 grid points), and the wavelength is 2.5 km, which is 1/8 of the model width. The bottom boundary is designed to follow the sinusoidal shape, and y_0 in equation (25) takes half grid size. In this case, all other elements have rectangular shape except the lowest row at the base. The interface between two materials crosses elements (Fig. 5). The high resolution is required to refine the sinusoidal geometry to be comparable with analytical solutions. As the relative fluctuation range does not vary too much with model resolution (Fig. 2b), the high-resolution models still have the issue of stress perturbations.

Free slip boundary conditions are applied to all boundaries except the bottom, where vertical velocity is prescribed

$$V_y = V_0 \sin\frac{2\pi x}{\lambda} \tag{26}$$

where $V_0 = 0.5 \text{ cm yr}^{-1}$. With the stream function method, Ramberg (1962) gave the functional form for the shear stress

$$\sigma_{xy} = 2V_0\omega^2 y e^{-\omega y}\cos(\omega x) \tag{27}$$

where $\omega = \frac{2\pi}{\lambda}$.

Comparing the numerical results with analytical results at y = 3dy, where dy is the spatial resolution in y direction, Fig. 6 shows the results processed by the Post-local projection, GHM, UnE and AGP methods. The worst results happen at the situation of pure Post-local without any pre-processing procedure, and several orders of magnitude differences between the analytical and numerical solutions occur around where the peak value is (Fig. 6a). Generally, all other cases with the application of a pre-processing method have damped the stress misfit error at $n\lambda \leq x \leq (n + 1/2)\,\lambda$, where n is integer (Fig. 6b, c & d). For the pre-processing methods, the maximum error for the UnE method is 31%, and the GHM method is 17%. The best one comes from the AGP method where the misfit at peak values are less than 0.4%.

Particularly, we further test the best choice δ used in AGP. The sampling radius used in Fig. 6d is equal to one element size. Comparing with other choices of sampling radius (Fig. 7), we find the maximum misfit between numerical results and analytical solutions quickly decreases from half to one element length for both the observation at y = 3dy and 4.5dy, and the misfit slightly varies with the sampling radius when it is larger than one element size. For the observation at y=3dy, It is consistent with our conclusion in section 4.1 that the end-member case of the AGP method that has an extremely large sampling area produces the same effect of the UnE method (Fig. 6b), which generates worse results than the AGP method with $\delta/dx \cong 1$ (Fig. 6d).

This trend of maximum misfit versus sampling radius in models with Q_2 elements is consistent to that observed in models with Q_1 elements (Fig. 7). The mesh has 160×160 Q_2 elements. The thickness of the thin layer (0.25km) also spans 2 grid size (5 grid points), and the wavelength is 2.5 km, which is 1/8 of the model width. The maximum misfit drops from more than 1×10^4 Pa to less than 7×10^3 Pa when the sampling radius increases from half to one element length for both observations at y = 3dy and 4.5dy, after which the maximum misfit does not vary significantly with sampling areas. In this case, the optimal sampling radius for AGP method is around one element length, which is same as that for Q_1 elements.

Additionally, two other averaging methods, the arithmetic mean and geometric mean, are tested in the AGP method instead of the harmonic mean used in equation (21). For a positive sequence $\eta = (\eta_1, \eta_2, \ldots, \eta_n)$, the arithmetic mean ($An$) and the Geometric mean (Gn) are defined respectively by

$$An(\eta) = \frac{1}{n}\sum_{i=1}^{n}\eta_i \quad \text{and} \quad Gn(\eta) = \frac{1}{n}\prod_{i=1}^{n}\eta_i \tag{28}$$

The harmonic mean defined in equation (20) is referred to as Hn. It is well known and has been demonstrated by Xia et al. (1999) that for the same sequence, $An \geq Gn \geq Hn$. The misfit of AGP method with An and Gn yields a maximum misfit (not shown in figures) that is close to that with the default Post-local projection (Fig. 6a), which has 2-3 orders of magnitude in difference between the numerical and analytical solutions. This indicates that the harmonic mean averaging method (Hn), which gives more weight to smaller values in the selected dataset, may be preferred to describe the interface between two materials of great contrast in strength.

4.1.3 SolCx model

The SolCx benchmark model is used by Thielmann et al. (2014) to test the influence of sharp viscosity jump within one element on computation error and convergence rate. The SolCx benchmark is a complementary case that includes the body force terms while that is not considered for both simple shear and folding models. We use the model setup from Thielmann et al. (2014) to compare the AGP pre-processing method with their sophisticated least square interpolation method, which is referred to as T2014 model in the next context. The analytic solution is derived by (Zhong, 1996), and the code for this analytic solution is included in the Underworld package.

The model is a unit box with a viscosity jump of 10^3 at x=0.5, and density is described by the trigonometric function $\rho = \sin(\pi y)\cos(\pi x)$, and the gravity is 0 in the x direction and 1 in the y direction (Fig. 8). The mesh is composed of 51×51 Q_2 elements, forming 103×103 calculation nodes. The AGP pre-processing method with the sampling radius of one element length is applied to compare with T2014 model results. The Harmonic-mean method is utilized to average particle properties to gauss point. Free-slip boundary conditions are applied to four edges.

The numerical results of velocity, shear stress and pressure field are shown in Fig. 9a-9d. The corresponding error in Fig. 9e-9h is the absolute difference between the analytic and numeric solutions. The maximum absolute error in our results is 2×10^{-5} for V_x and 2.5×10^{-4} for V_y, which is much lower than that in the T2014 model (1.4×10^{-4} for V_x and 5×10^{-4} for V_y). However, the error for pressure field in our model is about twice of the T2014 model. The maximum shear stress error (8.8×10^{-3}) occurs to the interface in our model, but T2014 model does not provide their stress data for comparation. The T2014 model uses least square interpolation which requires the calculation of the inverse of a matrix, same as the SPR or the Post-global method. Enforcing continuity through the least squares fit may introduce the over-shooting or under-shooting issues, which produce properties at quadrature points or nodes of significantly large (or small) values relative to the maximum (or minimum) value of the physical properties on particles (Thielmann et al., 2014). Therefore, the AGP pre-processing method is a much more straightforward and robust implementation than the least square interpolation used in the T2014 model.

Instead of the harmonic-mean averaging method, with the arithmetic-mean averaging, we find the maximum shear stress error is reduced to 5×10^{-3} (Fig. 10). In this case, the arithmetic-mean may be more suitable than the harmonic-mean averaging method. Shear stress errors at x=0.51 for different methods are illustrated in Fig. 10c. The difference caused by arithmetic and harmonic mean may be explained by their physical meanings proposed by Schmeling et al. (2008), who suggested that the harmonic-mean averaging best represents the effective viscosity of simple shear models, while the arithmetic-mean averaging can stand for the effective viscosity of pure shear models. The SolCx model is driven by body force rather than the surface drivers in simple shear models and folding models. Accordingly, the SolCx model may be dominated by the pure-shear mode and the other two models in section 4.1 and 4.2 are by the simple shear mode. In real cases, complex geological models are often composed of both end-member cases. Thus, the choice of arithmetic or harmonic mean depends on the specific geologic problems. However, we further apply the SPR post-processing method on those results obtained by the AGP pre-processing method with harmonic mean averaging, and the final accuracy can reach the same level as the AGP with arithmetic-mean method (Fig. 10). Therefore, the AGP pre-processing with harmonic averaging plus the SPR post-processing method could be a practical option for models when we are not familiar with the dominating deformation mode (simple shear or pure shear). Alternatively, it is worthwhile to consider the transversely isotropic viscosity that takes different averaging method for the viscosity in different directions in the future work.

4.2 Models without analytical solutions

Models in sections 4.1 are all based on a relatively simple geometry, the stress field of which can be obtained through analytical solutions, and the precision of numerical results have been checked by plotting against corresponding analytical solutions (Fig. 6 & 9). In this section, we test models that do not have a relatively simple analytical solutions as those in section 4.1. First, we test a model with a fault (thin weak zone) that is at a low angle to the x-axis. Then, we build a synthetic model by using the observations from a complex fault network to test how the methods proposed in this study work in a complex system that does not have analytical solutions.

4.2.1 Fault at a low angle to *x*-axis

The model tested here is close to that investigated in section 4.1.1 and has a weak zone ($\eta_2 = 10^{18}\, Pa \cdot s$) embedded in a relatively strong background ($\eta_1 = 10^{20}\, Pa \cdot s$). The setup is shown in Fig. 11. With the top boundary fixed, the driving velocity V_0 at bottom is 1 cm yr^{-1}. The velocity at both lateral boundaries linearly increases from 0 cm yr^{-1} (top boundary) to 1 cm yr^{-1} (base boundary). The fault (~160 m thick) is at ~10° to the *x*-axis, thus containing rectangular elements that has both strong and weak materials (Fig. 11a). We also build a model that has mesh edges aligned with the material interfaces (Fig. 11b) and the mesh in the y-direction surrounding the weak zone is refined, with the grid size varying from 0.21 m to 330 m. We take the aligned case as a reference model and the results may represent analytical solutions due to high resolution and body fitted mesh.

The reference model demonstrates smooth stress field along the fault (Fig. 11c), while the default Post-local projection has intensive perturbations along the fault (Fig. 12). Besides the absolute value of the stress field (left panel in Fig. 12), we also calculate the relative differences between the reference model and the case that contain elements with a mix of materials (right panel in Fig. 12). All pre-processing methods can help mitigate stress perturbations as that in section 4.1. The relative difference between the Post-local projection without any pre-processing and the reference model is high (0.6-1.0) along the fault. After adjusting material contrast in elements with pre-processing methods, the difference is reduced to be 0-0.2, though some light spots (high difference) occur along the fault. In this case, the global method with harmonic-mean averaging (GHM) seems to produce better results than averaging at Gauss quadrature points (AGP). For those light spot, further application of the superconvergent point recovery method (SPR) may help alleviate it as shown in section 4.1. It is worthwhile noting that, with the SPR method, we can reconstruct continuous stresses on specified patches rather than on the whole domain. It is convenient to use the patch recovery method on specified areas of anormal stress. In cases of 150×75 Q_2 elements, the results with the pre-processing procedure are not better than the Q_1 cases (not shown in figures). When the yield stress (e.g., the upper limit of the stress is a constant value of $10^{6.1}$ Pa) is applied, it is found to produce a smooth stress field. That means those high stress perturbations along the fault are forced to be damped to be less than the yield stress, but this will cause another problem that regions may yield when the expected stress is lower than the yield value, which may affect fault branches development in the long-term deformation.

4.2.2 Complex fault geometries

The case study of a complex fault geometry is based on the San Andreas Fault system in California. The San Andreas Fault (SAF) System has received the most in-depth study around the world, and scientific publications about the San Andreas Fault System from 1991-2013 produced about 3400 peer-reviewed articles (Gizzi, 2015), i.e., almost a paper is published every other day. The San Andreas Fault strikes through the state of California and is a transform boundary between the Pacific and North American plates. Many studies have suggested that the San Andreas Fault at different segments accommodates 20-75 % relative motion between these two plates (~50 mm yr^{-1}) (Atwater and Stock, 1998; DeMets and Dixon, 1999; Meade and Hager, 2005). We map the major faults based on the WGCEP (2007 Working group on California Earth-quake Probabilities) fault traces, where only major fault traces with long-term strain rate of orders of magnitude higher than that of less deformed areas are selected (Bird, 2009) (Fig. 11). The 2-D model is 1110 km long and 484 km wide with the Q_1 element a resolution of 400×200. A simple shear boundary condition is applied to y = 0 km (V_x = 4 cm yr^{-1}) and y = 484 km (V_x = 0 cm yr^{-1}), and the velocities at two lateral boundaries linearly decrease from 4 cm yr^{-1} at y = 0 km to 0 cm yr^{-1} at y = 484 km. The fault area generally spans 3 – 5 grid points, and the viscosity for the mapped fault area is set to be a constant value of 10^{19} Pa•s. The viscosity of non-fault area is 10^{23} Pa•s.

The second invariant stress of the viscous model in Fig. 13 shows significant differences between the raw result and the one with the AGP pre-processing method with the sampling radius of one element length. Stress perturbations occur along the San Andreas Fault (SAF, x = 250 – 500 km) and the Garlock Fault (GF; y = 150 km – 400 km) for the raw output with default Post-local projection. With the AGP pre-processing method applied, a smooth stress field is observed along the SAF and GF. The stress perturbation along the San Andreas Fault and Garlock Fault in the raw output is one to two orders of magnitude higher than that the smooth results. Although the analytical solution is unable to be obtained here for the complex fault system, with benchmarks in section 4.1, we suggest that the results processed with AGP pre-processing method is supposed to have higher precision than the raw result. From the AGP result, we find that the areas surrounding fault tips are of high stress, while the areas close to and along the major fault traces (the San Andreas Fault or Garlock Fault) are of low stress. However, the convex side of bending area (the intersection between the San Andreas Fault and Garlock Fault) is also at a higher stress state than those at straight segments. The East California Shear Zone (ECSZ) where there are arrays of sub-parallel fault traces are in a low stress state. We note that, although this is only a 2-D simplification and all faults are of the same strength (viscosity), the emergent stress field has been so complex due to the interaction of a fault network.

5 Conclusions

We compare the effects of both post-processing and pre-processing methods in dampening down stress perturbations, which are introduced by mixed materials of strength contrast in one element for the Particle-in-cell Finite Element method. The classical post-processing methods alone cannot eliminate stress oscillations. Instead, with the pre-conditioning methods to reduce the interface strength contrast first, the Post-local method can generate a relatively accurate stress field close to analytical solutions. For the pre-conditioning methods, the global method with harmonic-mean averaging method (GHM) uses the least computational cost, but only helps reduce noises in models interpolated with Q_1 element rather than Q_2 element. Both methods of unification of properties in one element (UnE) and averaging at gauss quadrature points (AGP) need look for mixed-material cells first, but the AGP method takes more time in finding and averaging particles within specified distances to the gauss integration point. For the case of simple shear (fault is parallel to the velocity direction), the UnE method is the best option, but for other more generic models, the AGP method is the preferred. The optimal sampling distance to the gauss point is one element length for both Q_2 and Q_1 elements. For models dominated by pure shear mode, the arithmetic mean is better than the harmonic mean for the AGP method. Additionally, the classical superconvergent point recovery (SPR) method can be further utilized to refine results processed by combined pre-processing and Post-local methods, although the SPR method alone cannot effectively remove stress perturbations. The synthetic model test demonstrates that, with complex fault geometries, the AGP map can produce a relatively smoother stress field than that in a raw result with Post-local projection.

Acknowledgements

We thank Australian Research Council for funding this research under Discovery Grant DP170103350. Testing models are run with the assistance of resources from the National Computational Infrastructure (NCI), as well as the Pawsey Supercomputing Centre.

6 References

Atwater, T., Stock, J., 1998. Pacific-North America plate tectonics of the Neogene southwestern United States: an update. International Geology Review 40, 375-402.

Bird, P., 2009. Long‐term fault slip rates, distributed deformation rates, and forecast of seismicity in the western United States from joint fitting of community geologic, geodetic, and stress direction data sets. Journal of Geophysical Research: Solid Earth 114.

Braun, J., Sambridge, M., 1994. Dynamical Lagrangian Remeshing (Dlr) - a New Algorithm for Solving Large-Strain Deformation Problems and Its Application to Fault-Propagation Folding. Earth and Planetary Science Letters 124, 211-220.

DeMets, C., Dixon, T.H., 1999. New kinematic models for Pacific-North America motion from 3 Ma to present, I: Evidence for steady motion and biases in the NUVEL-1A model. Geophysical Research Letters 26, 1921-1924.

Deubelbeiss, Y., Kaus, B.J.P., 2008. Comparison of Eulerian and Lagrangian numerical techniques for the Stokes equations in the presence of strongly varying viscosity. Physics of the Earth and Planetary Interiors 171, 92-111.

Gizzi, F.T., 2015. Worldwide trends in research on the San Andreas Fault System. Arabian Journal of Geosciences 8, 10893-10909.

Harlow, F.H., 1964. The particle-in-cell computing method for fluid dynamics. Methods Comput. Phys. 3, 319-343.

Hinton, E., Campbell, J.S., 1974. Local and global smoothing of discontinuous finite element functions using a least squares method. International Journal for Numerical Methods in Engineering 8, 461-480.

Hughes, T.J.R., 2012. The finite element method: linear static and dynamic finite element analysis. Courier Corporation.

Lenardic, A., Moresi, L.N., Mühlhaus, H., 2003. Longevity and stability of cratonic lithosphere: Insights from numerical simulations of coupled mantle convection and continental tectonics. Journal of Geophysical Research: Solid Earth 108, n/a-n/a.

May, D.A., Moresi, L., 2008. Preconditioned iterative methods for Stokes flow problems arising in computational geodynamics. Physics of the Earth and Planetary Interiors 171, 33-47.

Meade, B.J., Hager, B.H., 2005. Block models of crustal motion in southern California constrained by GPS measurements. J Geophys Res-Sol Ea 110.

Moresi, L., Dufour, F., Muhlhaus, H.B., 2003. A Lagrangian integration point finite element method for large deformation modeling of viscoelastic geomaterials. Journal of Computational Physics 184, 476-497.

Moresi, L., Quenette, S., Lemiale, V., Meriaux, C., Appelbe, B., Muhlhaus, H.B., 2007. Computational approaches to studying non-linear dynamics of the crust and mantle. Physics of the Earth and Planetary Interiors 163, 69-82.

Moresi, L., Zhong, S., Gurnis, M., 1996. The accuracy of finite element solutions of Stokes's flow with strongly varying viscosity. Physics of the Earth and Planetary Interiors 97, 83-94.

Ramberg, H., 1962. Contact strain and folding instability of a multilayered body under compression. Geologische Rundschau 51, 405-439.

Sadeghirad, A., Brannon, R.M., Burghardt, J., 2011. A convected particle domain interpolation technique to extend applicability of the material point method for problems involving massive deformations. International Journal for Numerical Methods in Engineering 86, 1435-1456.

Schmeling, H., Babeyko, A.Y., Enns, A., Faccenna, C., Funiciello, F., Gerya, T., Golabek, G.J., Grigull, S., Kaus, B.J.P., Morra, G., 2008. A benchmark comparison of spontaneous subduction models—Towards a free surface. Physics of the Earth and Planetary Interiors 171, 198-223.

Sulsky, D., Chen, Z., Schreyer, H.L., 1994. A Particle Method for History-Dependent Materials. Computer Methods in Applied Mechanics and Engineering 118, 179-196.

Thielmann, M., May, D.A., Kaus, B.J.P., 2014. Discretization Errors in the Hybrid Finite Element Particle-in-cell Method. Pure and Applied Geophysics 171, 2165-2184.

Wallstedt, P.C., Guilkey, J.E., 2011. A weighted least squares particle‐in‐cell method for solid mechanics. International journal for numerical methods in engineering 85, 1687-1704.

Xia, D.F., Xu, S.L., Qi, F., 1999. A proof of the arithmetic mean-geometric mean-harmonic mean inequalities. RGMIA research report collection 2.

Zhong, S., 1996. Analytic solutions for Stokes' flow with lateral variations in viscosity. Geophysical Journal International 124, 18-28.

Zienkiewicz, O.C., Zhu, J.Z., 1992a. The superconvergent patch recovery and a posteriori error estimates. Part 1: The recovery technique. International Journal for Numerical Methods in Engineering 33, 1331-1364.

Zienkiewicz, O.C., Zhu, J.Z., 1992b. The superconvergent patch recovery and a posteriori error estimates. Part 2: Error estimates and adaptivity. International Journal for Numerical Methods in Engineering 33, 1365-1382.

Figures

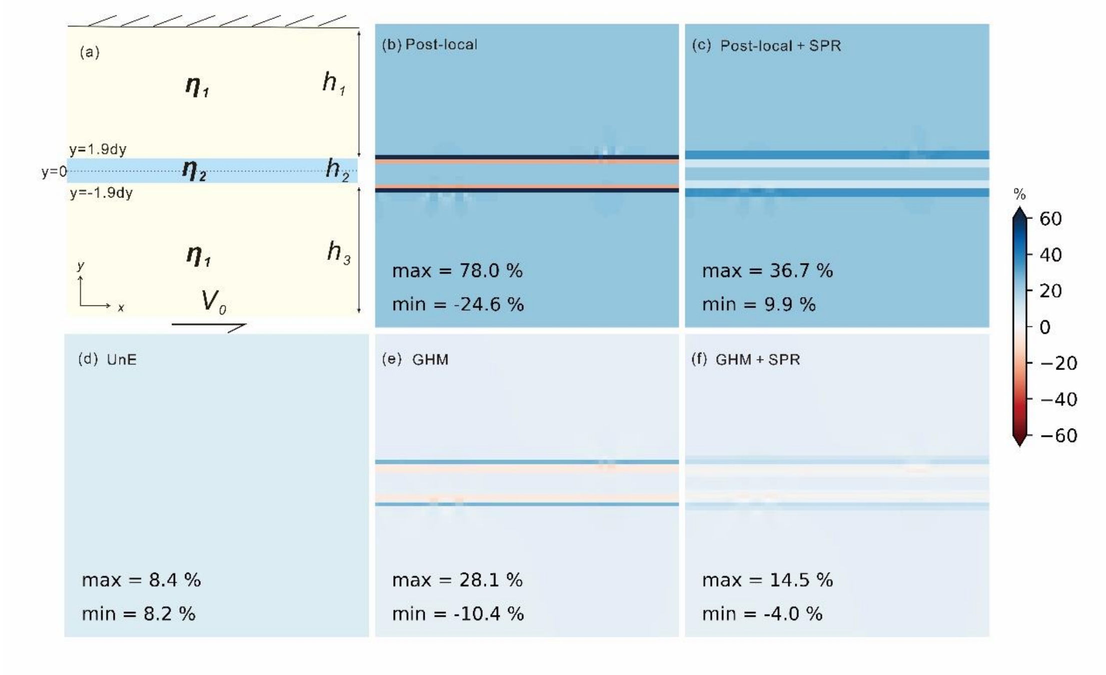

Figure 1. Simple shear model setup (a) and results of shear stress for Post-local projection (b), further applying SPR method on Post-local results (c), UnE pre-processing method (d), GHM pre-processing method (e), and post-processing with SPR on GHM results (f). The color bar shows the normalized relative error. The mesh consists of 80×80 regular Q_1 elements.

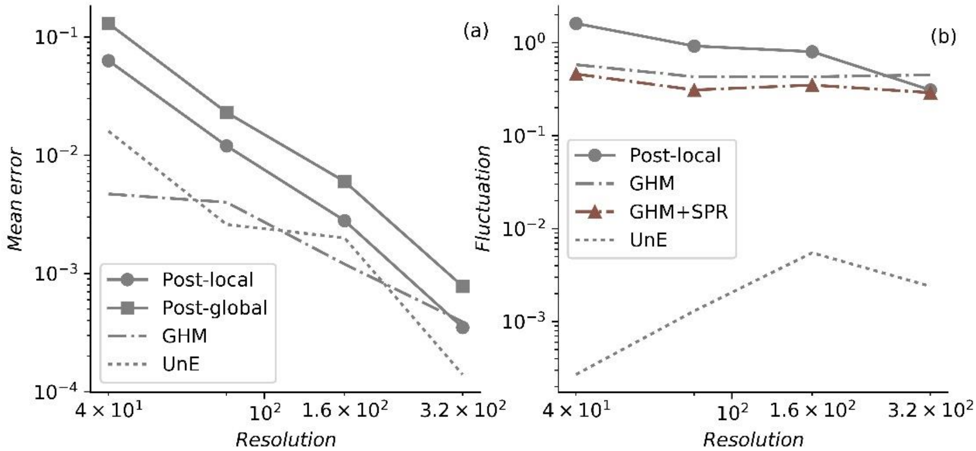

Figure 2. The mean error (a) and relative fluctuation range (b) versus resolution of element numbers.

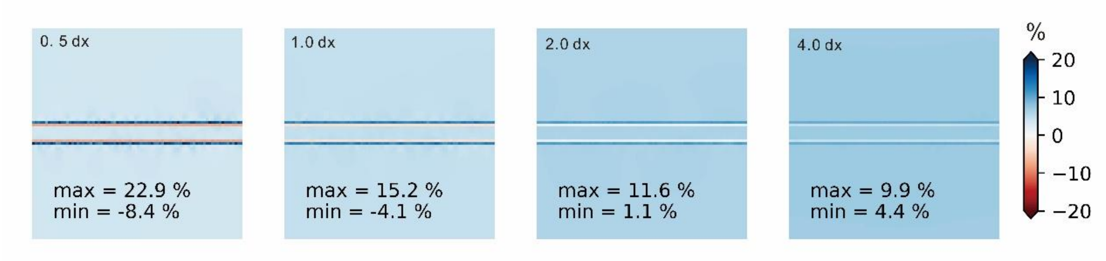

Figure 3. Recovered shear stress by using the APG pre-processing method with the sampling radius of 0.5 (a), 1 (b), 2 (c) and 4 (d) times of one element size. The color bar shows the normalized relative error. The mesh consists of 80×80 rectangular Q_1 elements. The relative error ranges decrease with sampling radius.

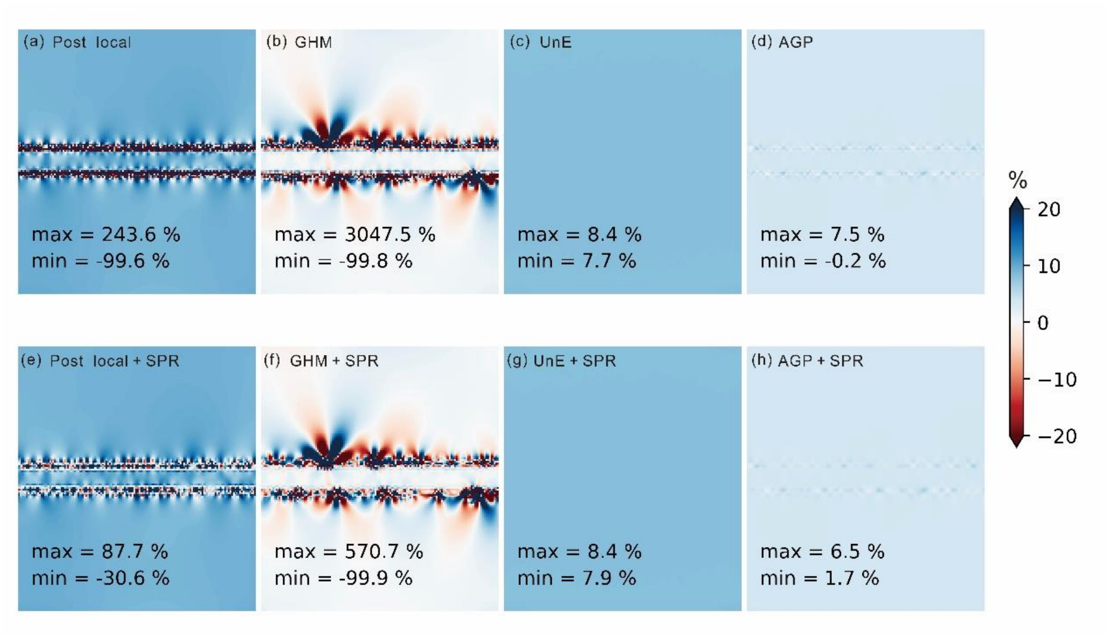

Figure 4. The simple shear model calculated with Q_2 element with the mesh resolution of 80 $\times$80. The upper panel shows results from the Post-local projection (a), and the pre-processing methods, including the GHM (b), the UnE (c), and the AGP methods (d); lower panel illustrates corresponding results after further processing with the SPR method. The color bar shows the normalized relative error.

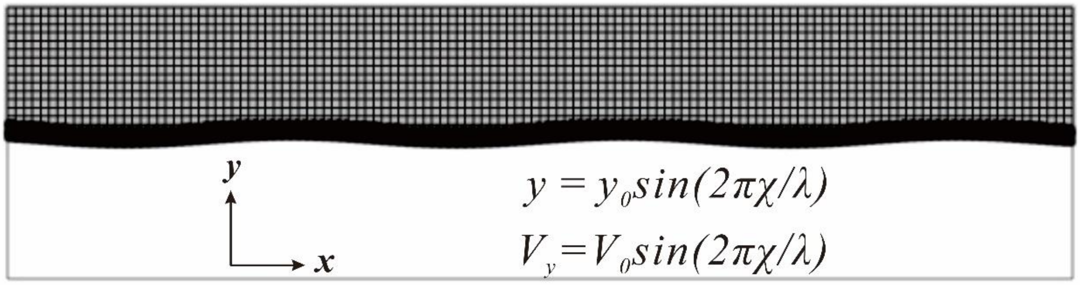

Figure 5. Sketch model setup that shows a thin sinusoidal competent layer (black) embedded in a background incompetent rocks (grey). The rectangular mesh is overlying the material field. This is only part of the model domain to show details of the mesh and mixed-material elements.

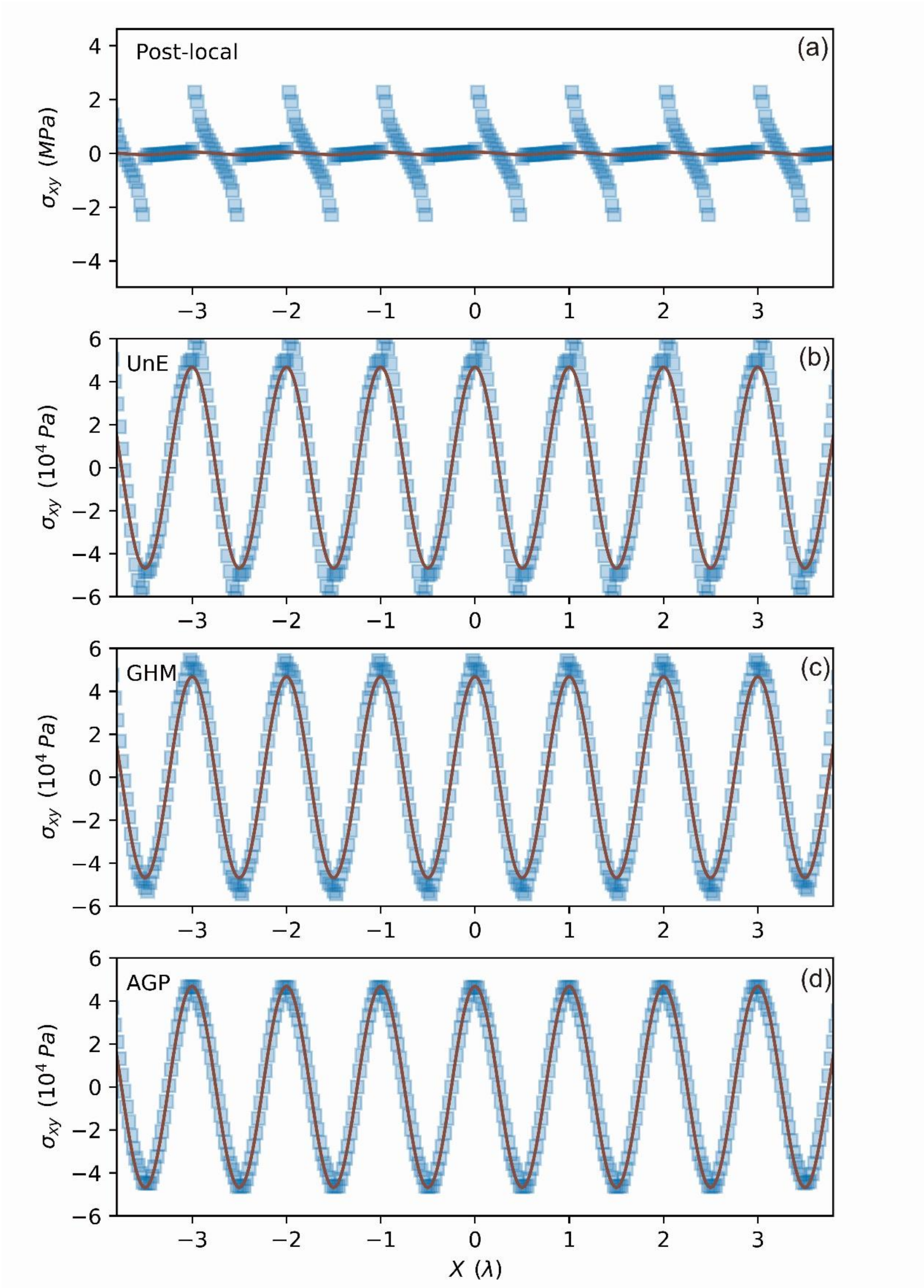

Post-local
(a)
σ_{xy} (MPa)
UnE
(b)
σ_{xy} (10^4 Pa)
GHM
(c)
σ_{xy} (10^4 Pa)
AGP
(d)
σ_{xy} (10^4 Pa)
X (λ)

590

Figure 6. Comparing analytical results for the folding model (solid line) with numerical solutions (square markers) that are processed with different methods: Post-local (a), UnE (b), GHM (c) and AGP(d). The sampling range in AGP is one element size.

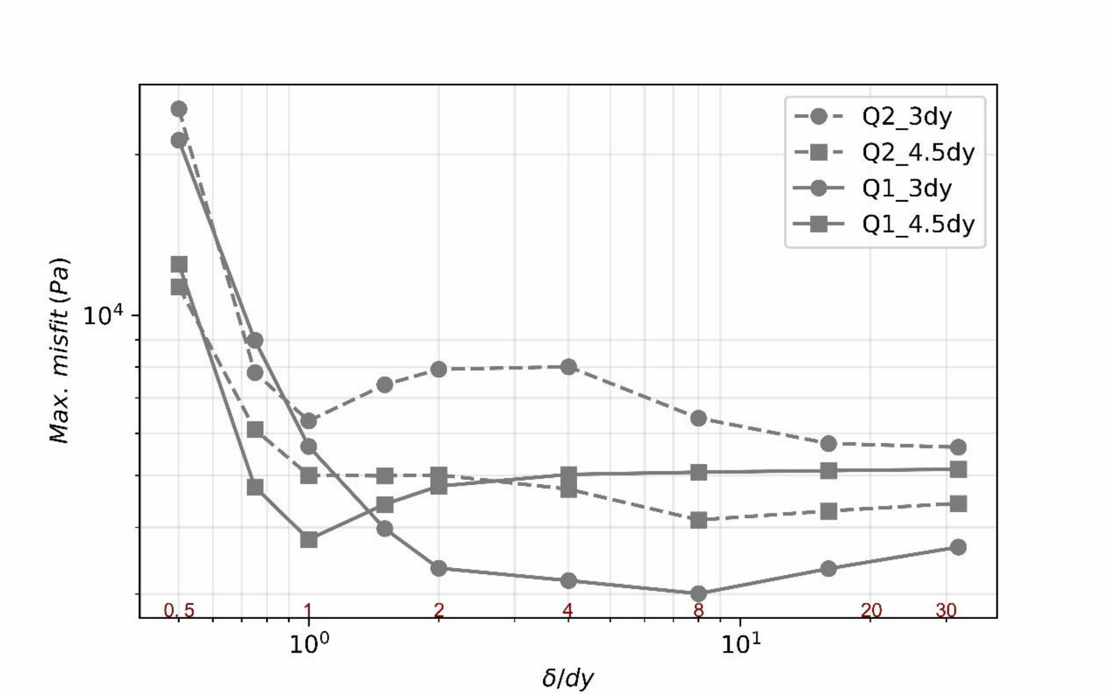

Figure 7. The maximum misfit between analytical solution for the folding model and results processed by the AGP method of different sampling radius for Q_1 (solid line) and Q_2 elements (dashed line). The mesh resolution for Q_1 is 320×320, Q_2 of resolution 160×160. The observation points are at y = 3dy and 4.5dy with the bottom of the model at y = 0.

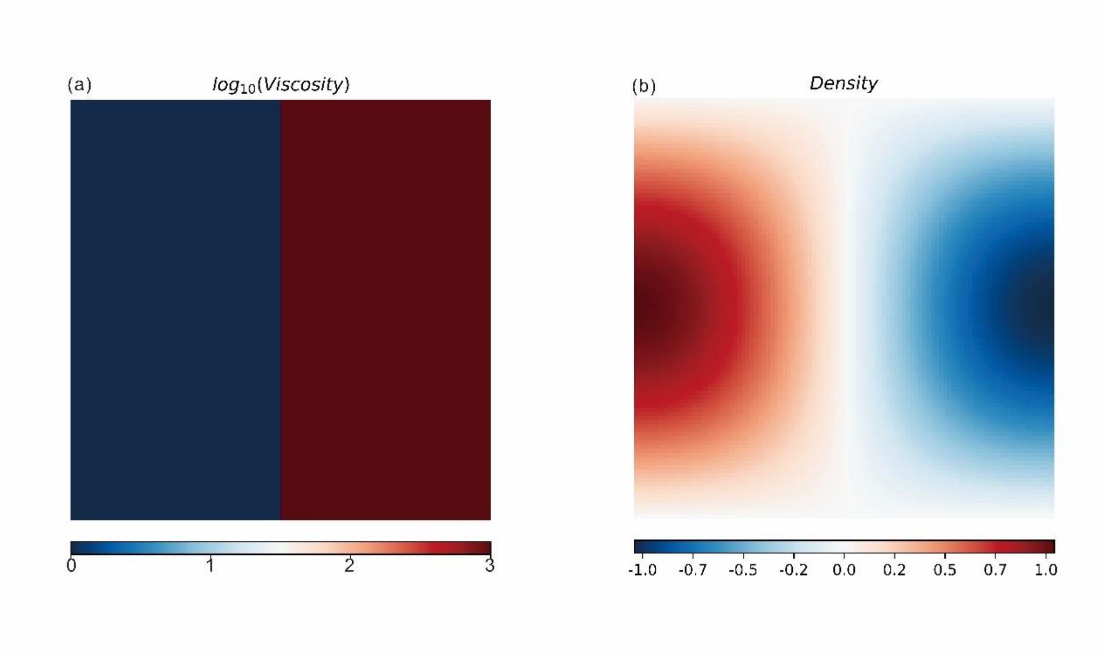

Figure 8. model setup for the SolCx benchmark.

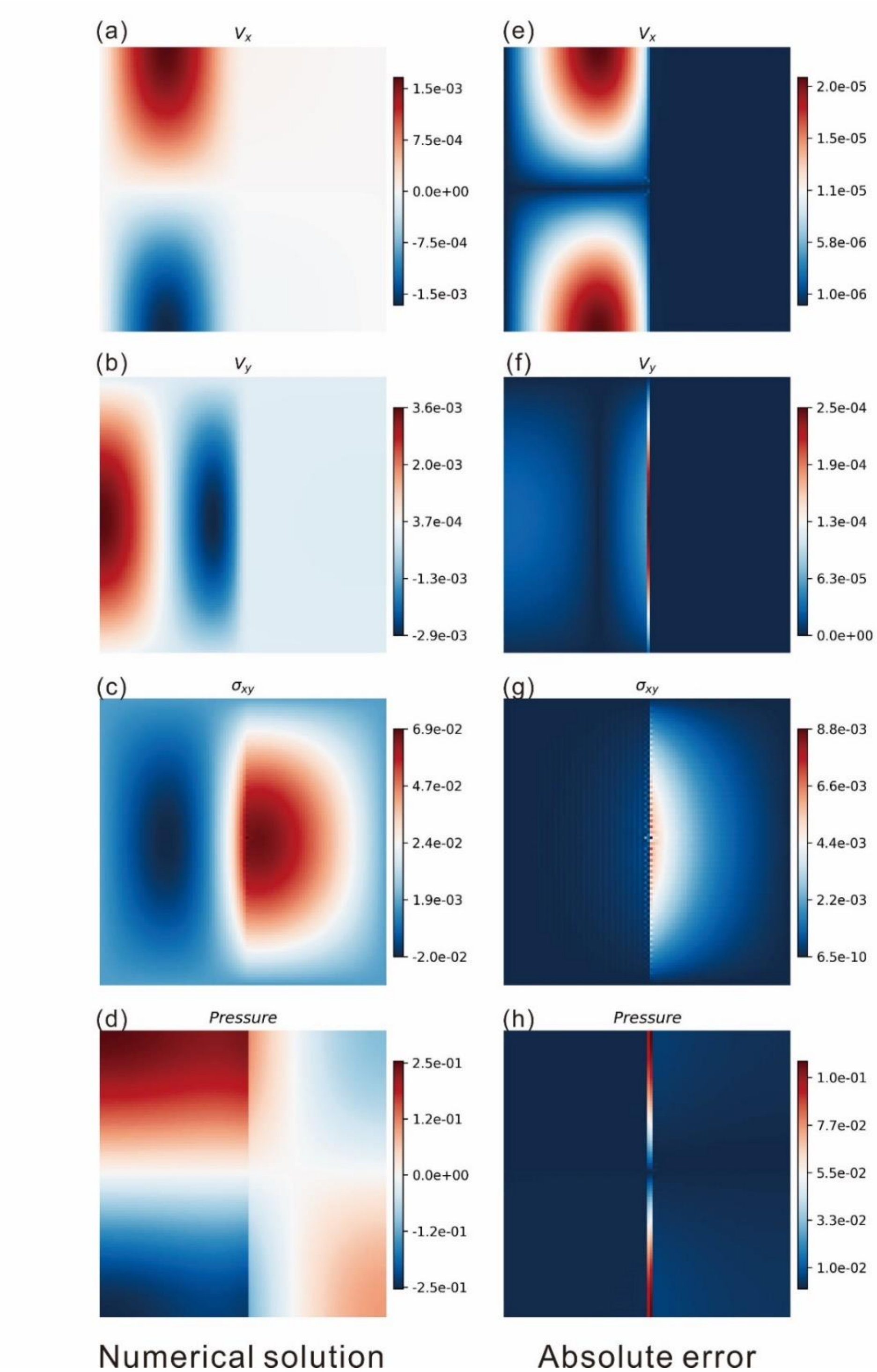

Figure 9. Left panel shows numerical solutions for V_x (a), V_y (b), σ_{xy} (c) and pressure (d) which are processed with the AGP method (search length is one element size), and right panel demonstrates corresponding absolute error.

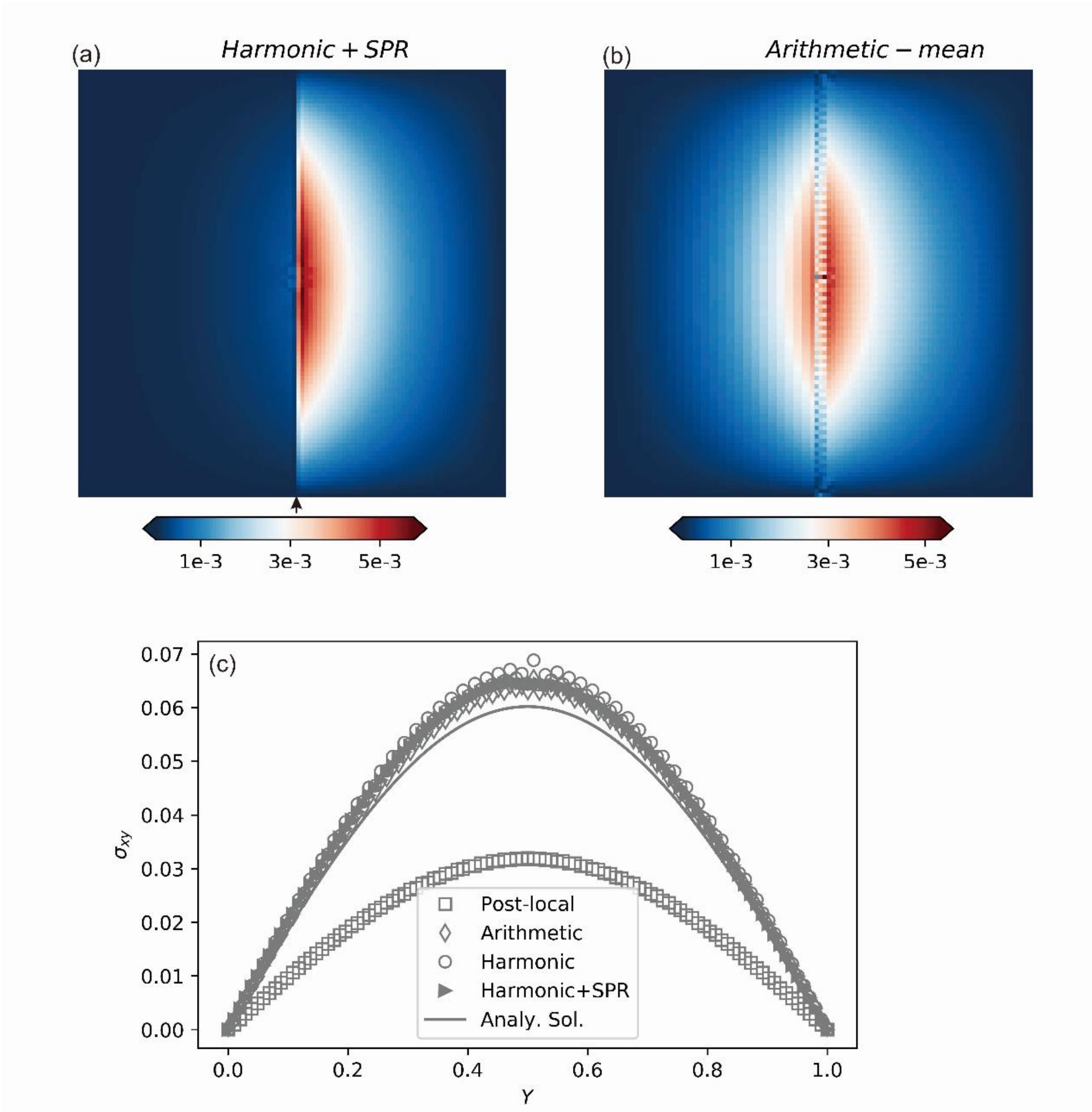

609

610 **Figure 10.** The absolute shear stress error for different methods: (a) applying SPR methods

611 to results obtained by the AGP method with harmonic mean, and (b) only AGP with arithmetic

612 mean. (c) The shear stress along the profile at x=0.51, the position of which is marked by an

613 arrow in (a), for different methods.

614

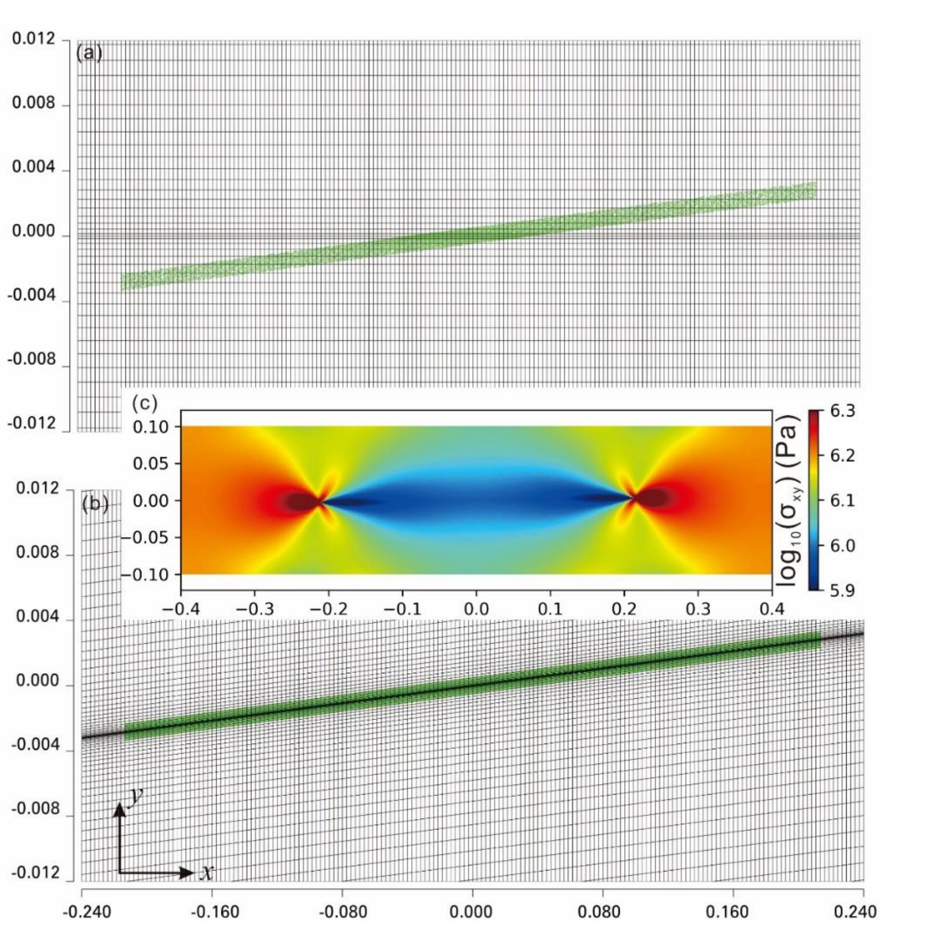

Figure 11. Models with an embedded weak zone (green particles at x=-0.21–0.21) that is at a low angle (~ 10º) to the *x*-axis. The model size is 80 km × 20 km, and the length shown here is normalized by 100 km. Q_1 elements of 300×150 is applied, and the mesh in the central part that is close to the weak zone is refined in y direction (a and b). The mesh edges in (a) is not aligned with the weak zone strike, while that in (b) is designed to be aligned with material interfaces. That means material mixing happens in (a) but not in (b). Note that the meshes in (a) and (b) are zoomed to see details of the mesh structure and are only part of the calculation domain. The whole-domain shear stress of the case in (b) is shown in (c). The results of the case in (a) is illustrated in Figure 12.

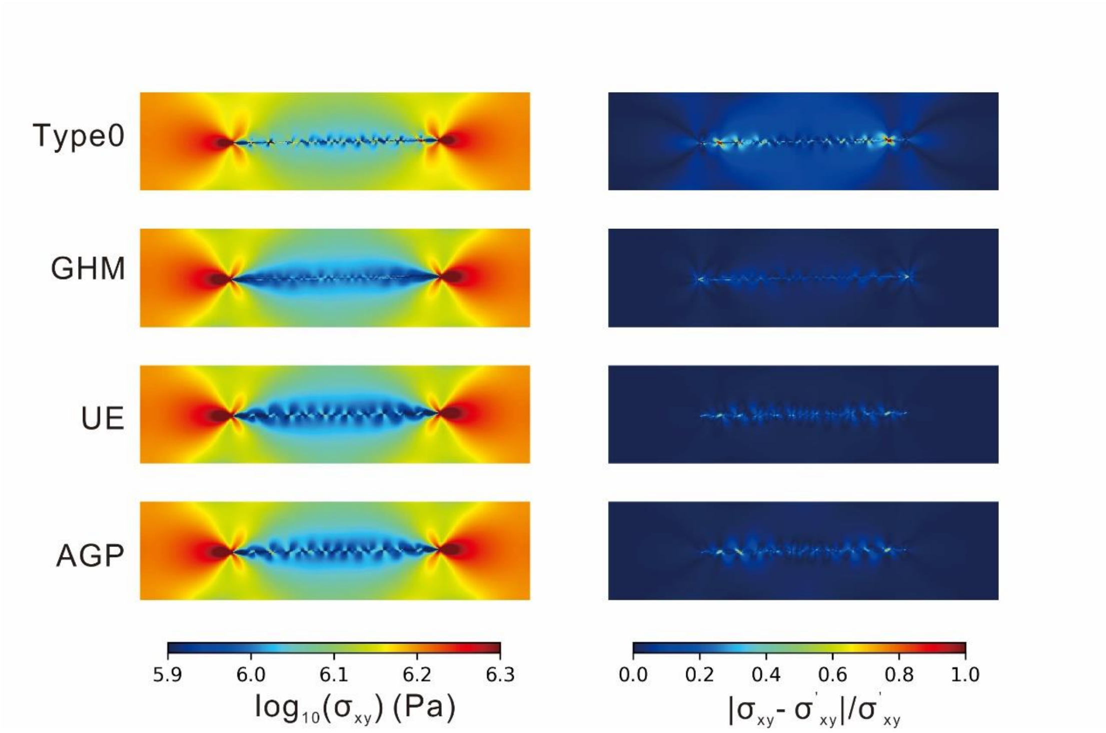

Figure 12. The results based on the mesh in Figure 11a. which has mixing materials in elements. The left panel shows absolute shear stress and the right panel shows the relative difference with respect to the reference model for different post- and pre-processing methods. σ'_{xy} is the stress in the reference model.

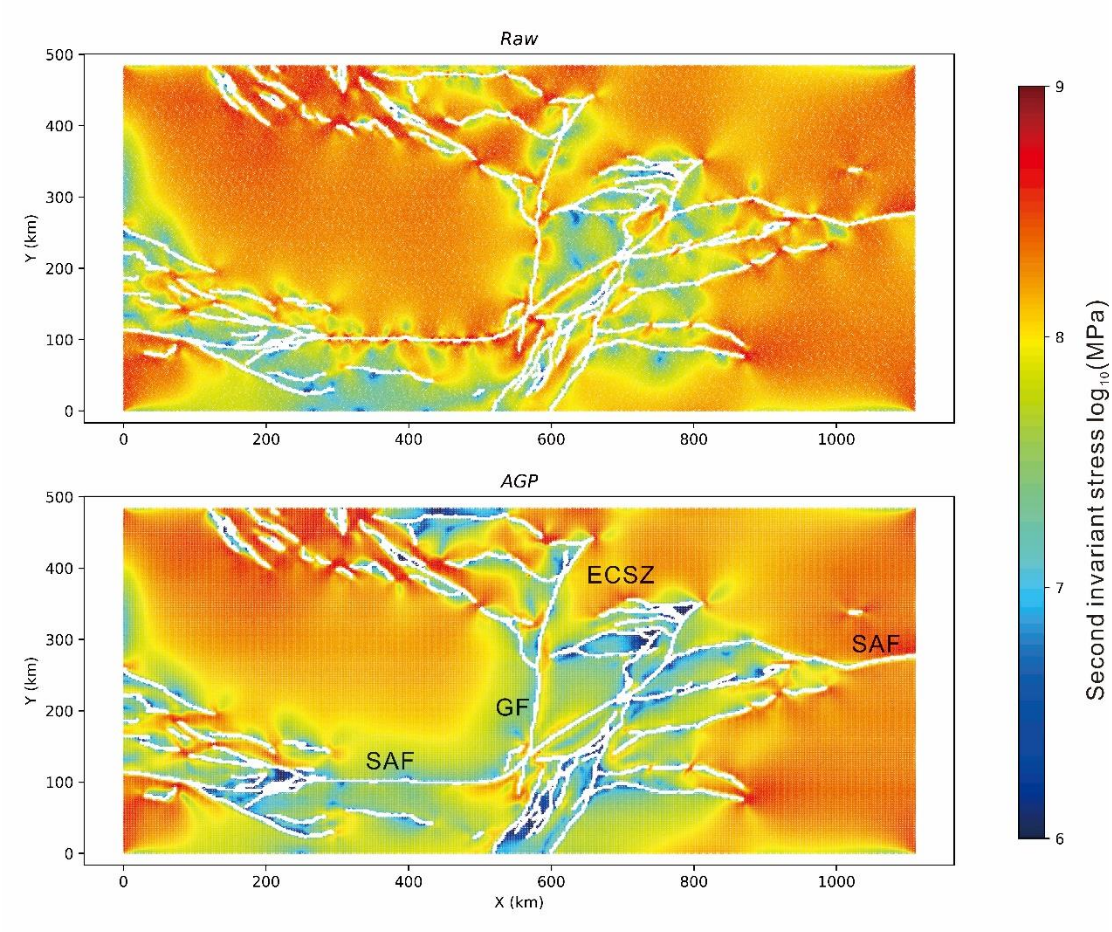

Figure 13. The second invariant stress of the synthetic model of complex fault geometries that are derived from the San Andreas Fault system in California (Bird, 2009). The white belts are the mapped faulting area, and only stresses in off-fault areas are shown. Briefs for major faults: SAF- San Andreas Fault, GF-Garlock Fault, ECSZ-East California Shear zone.